ADVANCED ENGINEERING MATERIALS
www.aem-journal.com

X-Ray Tomography Analysis of Damage Mechanisms in Metal Matrix Syntactic Foams During Compression

Indrajeet Tambe, János Endre Maróti, Imre Norbert Orbulov, Zoltan Hegedűs, Markus Ziehmer, Carl E. Krill III, Håkan Hallberg, Pär A. T. Olsson, and Johan Hektor*

The aim of this study is to explore the internal damage mechanisms of AlSi12 metal matrix syntactic foam (MMSF) with embedded ceramic hollow spheres (CHSs) to understand the damage behavior during compressive loading. To achieve this goal, in situ synchrotron X-ray tomography is used. A qualitative and quantitative assessment of the initiation and gradual collapse of matrix, filler material, and pores is presented. The imaging-based investigation provided detailed visualization and tracking of failure mechanisms of the MMSF, with emphasis on the collapse of hollow spheres at the microstructural level. The structural parameters describing performance limits are experimentally determined and correlated with internal mechanisms. It is concluded that a homogeneous distribution of the second-phase filler material results in a sequential collapse in a localized region; this leads to controlled and predictable energy absorption. The CHSs rupture is found to be location dependent within the localized shear band region, with spheres of all diameters failing to a similar extent. The results from this work can be used to train or validate predictive models of MMSFs deformed under compressive loading conditions by correlating the 3D damage progression with the overall mechanical response.

1. Introduction

Metal foams constitute a class of materials with unique properties, combining characteristics like low weight, high specific stiffness, and excellent energy absorption capability under deformation. They are categorized into three main groups: (I) open-cell foams, (II) closed-cell foams, and (III) foams produced with a secondary, hollow, or porous phase. The conventional metallic foams in groups (I) and (II) are comprised of a metal framework (the continuous metallic structure), stabilizing particles (fine particles that provide structural integrity and prevent premature collapse during production), and gas-phase bubbles in closed-cell foams or interconnected voids in open-cell foams. These materials are widely used in many applications, such as light-weight components and energy absorbers in automotive, aerospace, marine, and railway industries. However, issues persist during the foam production process, such as the collapse of gas bubbles due to insufficient melt viscosity or premature solidification, leading to irregular pore structures and weakened mechanical integrity.[1] There are also other challenges, for example, connected to maintaining structural stability, controlling cell size and distribution, and managing precise temperature control during the production process.[2] Because syntactic foams (group (III)) largely avoid these shortcomings, they have grown in importance, thanks to more effective production methods and good mechanical characteristics compared to other types of metal foams.

I. Tambe, P. A. T. Olsson, J. Hektor
Department of Materials Science and Applied Mathematics
Malmö University
20506 Malmö, Sweden
E-mail: indrajeet.tambe@mau.se

J. Endre Maróti, I. N. Orbulov
Department of Materials Science and Engineering
Budapest University of Technology and Economics
1111 Budapest, Hungary

The ORCID identification number(s) for the author(s) of this article can be found under https://doi.org/10.1002/adem.202501499.

DOI: 10.1002/adem.202501499

J. Endre Maróti, I. N. Orbulov
MTA–BME 'Momentum' High-performance Composite Metal Foams Research Group
Müegyetem rkp. 3., H-1111 Budapest, Hungary

Z. Hegedűs
Deutsches Elektronen-Synchrotron DESY
Notkestrasse 85, 22607 Hamburg, Germany

M. Ziehmer, C. E. Krill III
Institute of Functional Nanosystems
Ulm University
89081 Ulm, Germany

H. Hallberg
Division of Solid Mechanics
Lund University
PO Box 118, 22100 Lund, Sweden

P. A. T. Olsson
Division of Mechanics, Materials and Component Design
Lund University
PO Box 118, 22100 Lund, Sweden

Metal matrix syntactic foams (MMSFs) constitute a distinct class of metallic foams. They are unique composite materials consisting of a metallic matrix material, usually a lightweight alloy like aluminum[3,4] or magnesium,[5,6] and a second-phase filler. This filler can take the form of hollow elements, such as ceramic hollow spheres (CHSs) or microballoons, or porous materials like expanded perlite, clay, or glass.[7] MMSFs have gained attention due to their high energy absorption capability and attractive density-specific mechanical properties, finding application in fields like automotive collision damping and bullet- or blast-proof hulls, and they are contributing significantly to weight reduction in the transportation sector.[8–10] They can also operate at both elevated and cryogenic temperatures.[11,12] However, despite their widespread use, gaining a deeper understanding of the mechanical behavior of MMSFs remains an active area of research. An improved understanding of the internal damage mechanisms and quantification of structural parameters like compressive strength, fracture strain, structural stiffness, elastic energy absorption, and critical resolved shear stress are important for assessing a material's capability to withstand compressive loads.[13,14] From an engineering perspective, the onset of plastic deformation in MMSFs is also of the utmost importance, but it has yet to be studied in detail.

In recent years, reports in the literature have suggested that the intrinsic material structure of the filler, such as the volume fraction of hollow spheres and their composition, influences the mechanical properties of foams. For example, Kiser et al.[15] investigated the mechanical response of a set of MMSFs and discovered that the energy absorption capacity was extraordinarily high when compared to conventional metal foams. The enhanced absorption capacity was attributed to the controlled collapse of the hollow spheres. Building on this, Daoud[16] showed that syntactic foams containing a high volume fraction ($\geq$50 vol.%) of hollow spheres had a longer and flatter stress plateau than in specimens with a lower volume fraction of hollow spheres, because the structure provides more opportunity for hollow sphere walls to deform and collapse. The onset of failure phenomena in MMSFs was studied previously by conventional macroscale compressive tests equipped with (i) tactile extensometers,[7] (ii) acoustic emission devices,[17] and (iii) ex situ vibration analysis.[18] However, none of these works were able to determine the initial collapse and describe its subsequent evolution. Work has also been done on the modeling of MMSFs. Sanders and Gibson[19] developed models of the mechanical behavior of metal foams, suggesting that closed-cell foams have superior elastic modulus and strength compared to open-cell foams, particularly at high porosity. The elastic modulus and initial yield strength of MMSFs were also studied, revealing that the theoretical values of elastic modulus and strength are midway between those of open-cell and closed-cell foams. A similar model was developed by Marur[20,21] to determine the effective elastic modulus of a syntactic foam. This model considered imperfect interfaces between hollow spheres and the matrix. The results obtained using this model agree well with the measured elastic modulus reported in the literature.[22,23]

X-ray tomography is an effective tool to detect internal damage features in materials and structures.[24,25] It has been thoroughly investigated and utilized for various cases such as crack initiation and growth, fatigue and cyclic-load failure, and time-resolved defect evolution.[26–30] This technique has been further empowered by adding a fourth dimension to study the time-resolved material response under load, referred to as in situ testing. In situ experimental techniques using X-ray imaging provide information on the internal evolution of the material microstructure.[28,31,32] A detailed review of in situ experiments using X-ray tomography can be found in reference.[33] Since X-ray tomography can probe both the bulk and the surfaces of samples, their different mechanical response to applied strain can be studied. This has been utilized to study decohesion and crack propagation in the bulk and at the surface of SiC-reinforced metal matrix composites,[34] or void coalescence in aluminum alloys.[35] In both cases it was found that investigating only the surface led to large underestimation of the amount of damage in the samples. X-ray tomography of post-compression MMSFs also revealed that the interior (bulk) deformation behavior is different from that observed at the surface.[36] Hence, characterization methods with high spatial resolution probing the interior of samples are needed to study damage mechanisms in many types of materials, not least MMSFs. In,[37] a type of MMSF was studied with X-ray tomography ex situ after compression testing to classify structural features. Most other related studies focus on more easily accessible polymer-based syntactic foams.[38–40] Localized deformation features, often described in the literature as crash bands, kink bands, or deformation bands, have also been studied in other types of cellular materials and foams.[41–43] The use of 3D X-ray tomography to monitor microstructure evolution during in situ experiments was explored and combined with 3D modeling in,[44] though not specifically applied to MMSFs.

The aim of this article is to investigate and elucidate the internal damage mechanism during compression of an AlSi12-based MMSF with embedded CHSs. The specimen is characterized using in situ X-ray tomography. The study focuses on qualitative visualization and quantitative characterization of the evolution and behavior of microstructural damage in the MMSF specimen. This includes analyzing the initiation and gradual collapse of the matrix, filler material and pores and their relation to macroscopic foam deformation. Concurrently, mechanical parameters such as the compressive strength, fracture strain, structural stiffness, critical resolved shear stress, and elastic energy stored during deformation are determined, and the reduction in porosity is evaluated throughout the deformation process. The purpose of this study is to extend our knowledge concerning the compressive behavior of MMSFs by leveraging advanced characterization techniques. The 3D images obtained from the latter contribute primarily to investigations of the physical mechanisms occurring in the interior of the foam matrix (e.g., microcrack interaction with CHSs) and provide new information on the chronology of the collapse phenomena of CHSs during increasing loading. The prime novelty of this manuscript is the application of in situ synchrotron X-ray tomography to explain the internal damage mechanisms of MMSFs, the qualitative and quantitative assessment of the initiation and gradual progress of failure, and the detailed visualization and tracking of failure mechanisms. By correlating 3D damage progression with the overall mechanical response, this work lays the foundation for validating predictive models of syntactic foam deformation under compressive loading conditions. In particular, the combination of global force-displacement data with time-resolved 3D tomography of shear

band formation, CHS rupture and densification provides both macroscopic benchmarks and microstructure descriptors that can be directly used to calibrate and validate micromechanical and finite element models of MMSF deformation.

2. Experimental Section

2.1. Materials, Sample Production and Initial Characterization

A commercial AlSi12 alloy was used as matrix material; its chemical composition is shown in **Table 1**. CHSs provided by Sphere Services Inc., made of mixed oxides consisting mainly of Al_2O_3 and SiO_2, were used as the porosity-establishing filler phase. The stiffness of the matrix material, corresponding to its elastic modulus, is 69 GPa. The CHSs are made from silica (≈70%, with elastic modulus of 73 GPa) and alumina (≈30%, 200 GPa), resulting in a stiffness of ≈110 GPa. The effective density of CHSs (including the empty space in the sphere interior) is 0.36 g cm^{-3}, their compressive strength under hydrostatic loading is 30 ± 4 MPa, and their melting point is 1050 °C, as provided by the manufacturer. The role of the filler phase is to effectively reduce the density of the component and determine the geometry of the pores to endow the material with the excellent specific properties typical of MMSFs. The density of the AlSi12 alloy is 2.65 g cm^{-3}. To achieve a lower bulk density of MMSFs, the volume fraction of the filler was set to the relatively high value of 64 vol.%. The initial surface morphology and chemical composition of the CHSs prior to the foam production process were studied using scanning electron microscopy (SEM) and energy-dispersive spectroscopy (EDS) in a Philips XL-30 SEM with an EDAX Genesis X-ray EDS detector.

The samples were produced by low-pressure liquid-state infiltration. First, the hollow spheres were preprocessed to sort out broken spheres. The hollow spheres were poured into ethanol, so that only the intact ones floated to the surface of the alcohol. The intact and dried hollow spheres were then poured into a steel mold with internal dimensions of 36 × 55 × 360 mm^3. On top of the hollow spheres, an Al_2O_3 insulating mat was placed, which served to separate the molten matrix material from the CHSs until the moment of pressurized infiltration. On top of this, a machined block of AlSi12 was placed, which was later melted to become the matrix material in the MMSF. The prepared mold was placed in a furnace. A schematic drawing of the mold positioned inside the furnace is shown in **Figure 1**.

After being sealed, the furnace was evacuated to a pressure of less than 1 mbar using a Leybold Trivac D8B type vacuum pump. During the subsequent heating step, a uniform temperature was maintained by three heating zones, and the temperatures of the matrix block and the CHSs were continuously monitored using two thermocouples. The melting temperature of the AlSi12 alloy is 575 °C and infiltration was performed at 625 °C (50 °C above the melting point), which is sufficient for the infiltration of the CHSs.[45] Once the melting of the matrix material was completed, it formed a liquid plug in the mold, which was separated from the CHSs by the insulating mat, maintaining the vacuum around the CHSs. Then, evacuation was stopped, and Ar gas at a pressure of 500 kPa was let into the system. The resulting pressure difference between the Ar pressure in the furnace and vacuum under the molten matrix plug in the mold forced the melt through the insulating mat and infiltrated the set of hollow spheres. The pressure difference was maintained for 30 s. However, infiltration cannot be completely perfect due to the high surface tension of the matrix and the very small capillaries between the touching CHSs. Therefore, small infiltration-related voids can occur. The mold was thereafter cooled in air, and then the cast block of MMSF was removed from the mold for further machining. Cylindrical specimens with a diameter of 1.5 mm and height of 2.7 mm were machined from the MMSF block for axial in situ compression tests.

Table 1. Chemical composition of the AlSi12 matrix (in wt.%).[57]

	Si	Fe	Cu	Mn	Mg	Zn	Al
AlSi12	12.830	0.130	0.002	0.005	0.010	0.007	balance

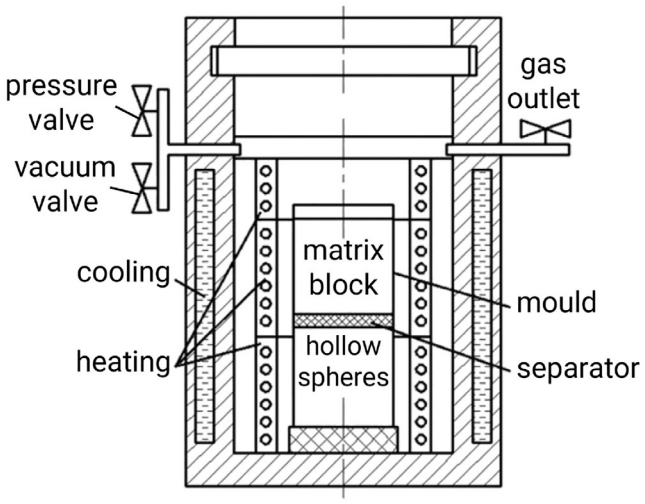

Figure 1. Schematic representation of the infiltration furnace.[7]

SEM images of the CHS filler material are shown in **Figure 2**. The CHSs in Figure 2a show a smooth and intact surface morphology, while in Figure 2b an intentionally broken CHS shows a dense and porosity-free wall. The outer diameter of the CHSs was measured to be 74 ± 12 μm, and their wall thickness was 3 ± 0.5 μm.

The porosity fraction, p_i, for an individual CHS with outer diameter d_o and wall thickness t_w can be calculated as

$$p_i = \left(1 - \frac{2t_w}{d_o}\right)^3 \quad (1)$$

Hence, for an individual CHS, 77.6 ± 4.8% is empty space, and the remaining 22.4% constitutes ceramic wall. The volume fraction of the inner void contributes to porosity. Now, when we consider all CHSs in the MMSF sample, the volume fraction occupied by all CHSs is $\nu_f = 64\%$. So, the overall porosity due to CHS voids in the MMSF sample can be computed from $P = p_i \cdot \nu_f$. Using this relation, the overall theoretical porosity in the MMSF sample caused by CHSs is calculated to be 49.7 ± 3.1%.

The chemical composition of the CHSs was measured by EDS, and the compositions in wt.% obtained for the different

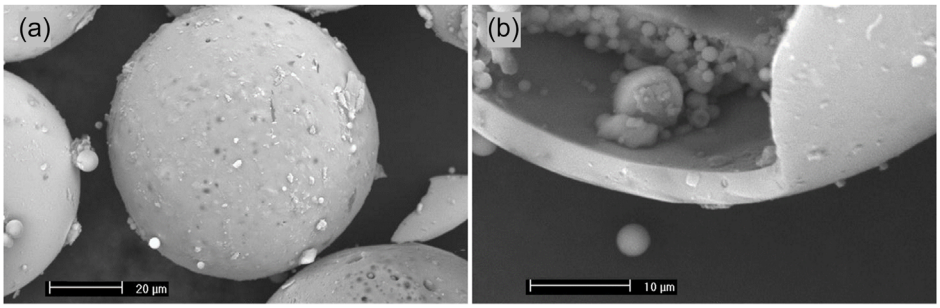

Figure 2. SEM images of filler CHSs: a) CHS with a smooth and intact surface and b) intentionally broken CHS, showing a dense and porosity-free wall.

Table 2. Chemical composition of the CHS filler material (in wt.%).

	SiO_2	Al_2O_3	TiO_2	Fe_2O_3	other oxides
Composition	58.0	38.5	1.6	0.4	balance

oxide types are listed in **Table 2**. The major oxide components were SiO_2 and Al_2O_3, but the material also contains small amounts of TiO_2, Fe_2O_3 and other oxides.

2.2. Experimental Setup

High-resolution X-ray tomography was used to map the internal damage occurring in MMSFs during compression tests. In situ compression experiments were carried out at the Swedish Materials Science beamline (P21.2) at PETRA III[46] with an incident X-ray beam of 37.5 keV and a beam size of ≈3.2 mm (horizontal) by 2 mm (vertical). Sample loading was carried out using a Deben CT20kN mechanical load frame. The experimental setup is shown in **Figure 3**.

For tomography measurements, a PCO Edge 5.5 camera was placed at a distance of 4.7 cm from the sample. The sample was rotated 360° around the fixed rotation axis of the Deben load frame, and radiographs were acquired in increments of 0.1° (i.e., 3600 projections per scan). The initial height of the sample (2.7 mm) was larger than the vertical beam size. Hence, two vertically overlapping scans were needed to cover the entire sample. Prior to loading, the compression platens were moved until they fully held the specimen, applying a minor seating force ($F \approx 5$ N). This was done to eliminate the effect of mechanical clearance in the displacement data. The first tomography dataset was recorded in the undeformed state of the sample, whereas subsequent tomographic characterization was performed after each increment of 50 µm compressive displacement, up to a total axial displacement of 1.70 mm. Each tomography scan took a total of 30 min. During this time, the displacement was held constant. In total, 34 tomographic volumes were recorded: one undeformed tomogram and 33 sequential tomograms after the incremental displacements.

2.3. Tomography Reconstruction and Segmentation

Prior to reconstruction, phase retrieval was performed using regularization parameter $\alpha = 0.001$ to optimize contrast and prevent artifacts at edges. The tomography data were reconstructed using

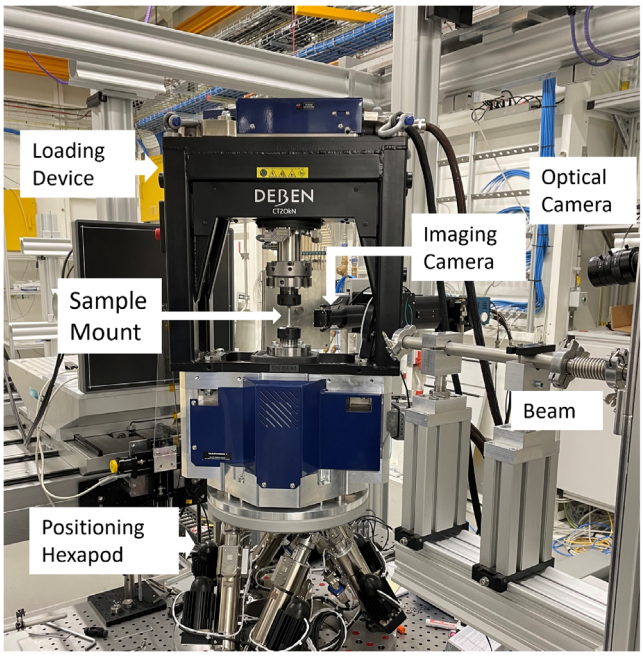

Figure 3. Experimental setup for in situ compression using Deben CT20kN load frame.

the Gridrec reconstruction algorithm[47] in the TomoPy Python module,[48] resulting in a 3D stack of grayscale images. The voxel size of the 3D reconstruction was 2.64 µm. The image stacks from the two vertically displaced layers were registered using the overlapping regions and merged to create a single image stack for each displacement step. This was carried out using the 3D image processing software Avizo (FEI Visualization Sciences Group).[49]

The matrix material and the internal hollow volume of the CHSs were segmented from the reconstructed tomography data. Thresholding was performed based on grayscale values to separate solid foam regions from porous regions. The hollow spheres that were open and touching the external boundary of the analyzed volume were removed. The porous regions were further labeled to identify the individual hollow spheres using image processing modules in the Python library SciPy.[50] Additionally, small infiltration-related voids that do not meet CHS shape and size criteria (sphericity < 0.85 and volume < 64 voxels) were excluded from the

labeled images using morphological and sphericity filters.[50–52] Each voxel of a 3D volume was classified either as matrix material, hollow sphere, or background for each load step. The labeled images were then used to calculate parameters like the volume and diameter of individual hollow spheres as well as the total microsphere volume. Calculation of these parameter values and generation of 3D visual images were carried out using Dragonfly software version 2022.2.0.1409 (Comet Technologies Canada Inc., Montreal, Canada).[53]

2.4. Shear Plane Angle Measurement and Critical Resolved Shear Stress

Each segmented 3D image was further processed to identify voxels inside the localized deformation zone, or shear plane. These voxels were identified using morphological and sphericity filters to find crushed CHSs. A plane was fitted to the 3D voxels in the localized deformation zone to trace the inclination of the identified deformed regions. This plane was used to determine the angle ψ between the normal direction of the fitted plane and the loading direction. A schematic illustration is provided in **Figure 4** to depict the shear plane region, the angle ψ, and the normal and shear components of the applied compressive force acting on the shear plane during displacement-controlled compression.

Using the maximal force to initiate a crack, F_p, and the initial cross-sectional area of the sample, A_0, the critical resolved shear stress, τ_{CRSS}, acting on the shear plane was calculated as shown in Equation (2)

$$\tau_{CRSS} = \frac{F'_p}{A_s} = \frac{F_p \cdot \sin(\psi) \cdot \cos(\psi)}{A_0} \quad (2)$$

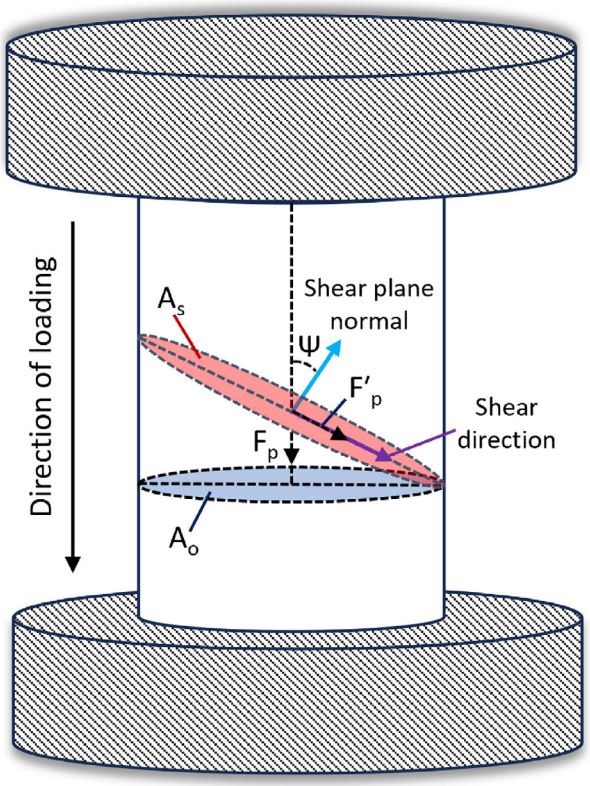

Figure 4. Schematic illustration of a cylindrical sample constrained by a fixed bottom and a displacement-driven top. Localized deformation occurs along the shear plane (shaded red region), where crushed pores coalesce into a crack. The angle ψ is between the shear plane's normal (blue arrow) and the loading axis. F_p is the maximal axial compressive force to initiate a crack.

3. Results and Discussion

3.1. Microstructure of Foams

The microstructure of the MMSF specimen was studied by using X-ray tomography to extract information about the distribution of the inner voids of the CHSs. The full 3D tomographic reconstruction of the as-prepared MMSF sample with labeled CHSs is shown in **Figure 5**a. 2D cross sections through the center of the sample are shown in Figure 5b,c. The color scale in Figure 5c represents the diameter of the pores: large pores are red and small pores are blue. The pore size distribution in the sample, before compression, is shown in Figure 5d. The mean diameter of the pores, corresponding to the inner void diameter of the CHSs, is 68 μm with a standard deviation of 24 μm. This corresponds to an outer diameter of 74 μm (assuming a 3 micron wall thickness), which agrees with the SEM estimate. The measured overall porosity due to CHSs was found to be 48.5%, which lies in close agreement with the previous estimate of 49.7%.

It is important to obtain a homogeneous distribution of the CHSs to ensure isotropic and constant materials properties of the MMSF. A 2D cross section through the center of the sample is shown in Figure 5e. The color map legend in Figure 5e represents the nearest-neighbor distance (NND) of the filler CHSs—i.e., the distance between the centroids of closest neighbor to its centroid. The NND distribution in the sample, before compression, is shown in Figure 5f. Visual inspection of Figure 5e, indicates a homogeneous distribution of CHSs, as the NNDs are spatially uniform in the sample. The distance distribution in Figure 5f shows one prominent hump rather than multiple peaks. Also, there is no visible clustering of CHSs in Figure 5b,c,e. Hence these results collectively confirm a homogeneous distribution of porosity due to CHSs in the sample.

3.2. Mechanical Behavior, Structural and Internal Response

The force-versus-displacement data gathered during the in situ compression experiment are shown in **Figure 6**a. The precise points at which loading was halted and tomography scanning occurred for each compressive displacement (δ) step are indicated by markers. The force initially increases linearly with applied compressive displacement until the matrix material yields and undergoes localized deformation. The corresponding porosity and energy density are shown as a function of displacement in Figure 6b. The energy density in the sample equals the

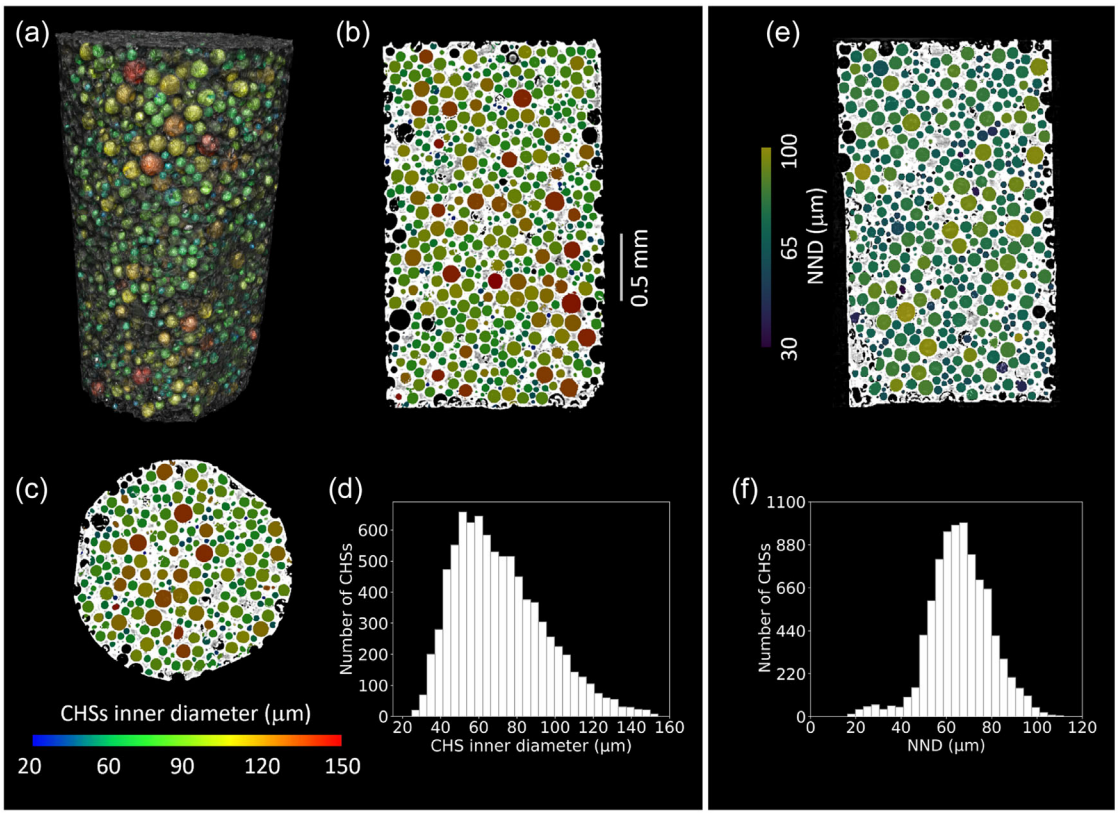

Figure 5. Tomography images of an MMSF: a) 3D representation of CHSs in the investigated sample with labeled CHSs; b) front view of the sample (middle plane); c) top view of the sample (middle plane); d) size distribution of CHS inner diameters from the initial tomographic scan of the sample in the undeformed state. The color map in the figure legend in (c) represents the equivalent-sphere inner diameter of the filler CHSs. e) Side view of the sample (middle plane), with color map describing the CHSs NND. f) The nearest neighbor-distance distribution of the filler CHSs from the initial tomographic scan of the sample in the undeformed state.

area under the recorded force-displacement curve normalized by the initial volume and can be integrated numerically.

The plots of force, porosity (caused by the intact spheres), and energy density versus displacement in Figure 6a,b are divided into five main regions. The 3D reconstructions of the investigated sample at selected displacement steps (one step for each of the five deformation stages) are shown in Figure 6c, illustrating the deformation of the surface during compression in each of the five stages. Cross-sectional tomography images of the sample at various stages of compression are presented in **Figure 7**, and the evolution of the localized deformation zone or the shear band region where CHSs are crushed during loading is shown.

In the first region (displacement 0 mm to 0.1 mm), the sample deformed elastically, and there was no crack or shear band formation. The overall deformation in this stage is related to the elastic deformation of the composite, with the slope representing the structural stiffness.[54] This quantity is one of the characteristic properties of MMSFs. In this loading region, the CHSs remained unharmed, so the overall porosity remains conserved, as observed in Figure 6b and 7a. This stage refers to the elastic regime.

In the second region (0.1 mm to 0.2 mm), the load transfer between the matrix and the CHSs increased to its maximum value when the force and corresponding stress reached the compressive strength of the sample. The associated displacement, δ_f, was used to calculate the fracture strain. The fracture strain, ε_f, is computed as δ_f normalized by the height of the sample. The force F_p was used to estimate the critical resolved shear stress, see Equation (2). F_p was followed by a decrease in the overall porosity caused by the rupture zone of CHSs. Upon reaching the force F_p, the first crack/shear band appeared in the sample, as shown in Figure 6c and 7b. The plane of the crack was at an angle $\psi \approx 47 \pm 2.7°$ with respect to the applied load direction. This agrees well with theoretical predictions for uniaxial loading[36] and experimental findings from previous studies.[7] This stage refers to shear band initiation.

In the third deformation stage (0.2 mm to 0.5 mm), the shear band expanded gradually, as shown in Figure 6c, and 7c,d. The neighboring CHSs broke layer by layer during further compression. This combined shearing-and-compression phenomenon dissipated a significant amount of mechanical energy, owing to the fracture of the CHSs, as shown in Figure 6b. This stage refers to sequential CHS rupture.

In the fourth region (0.5 mm to 1.2 mm), the shear band continued to expand, as shown in Figure 7e–g. Due to relative sliding in the shear band zone, as evident in Figure 6c, the force remained relatively constant. However, the sequential breaking of CHSs absorbed a large amount of energy. This stage refers to plateau behavior.

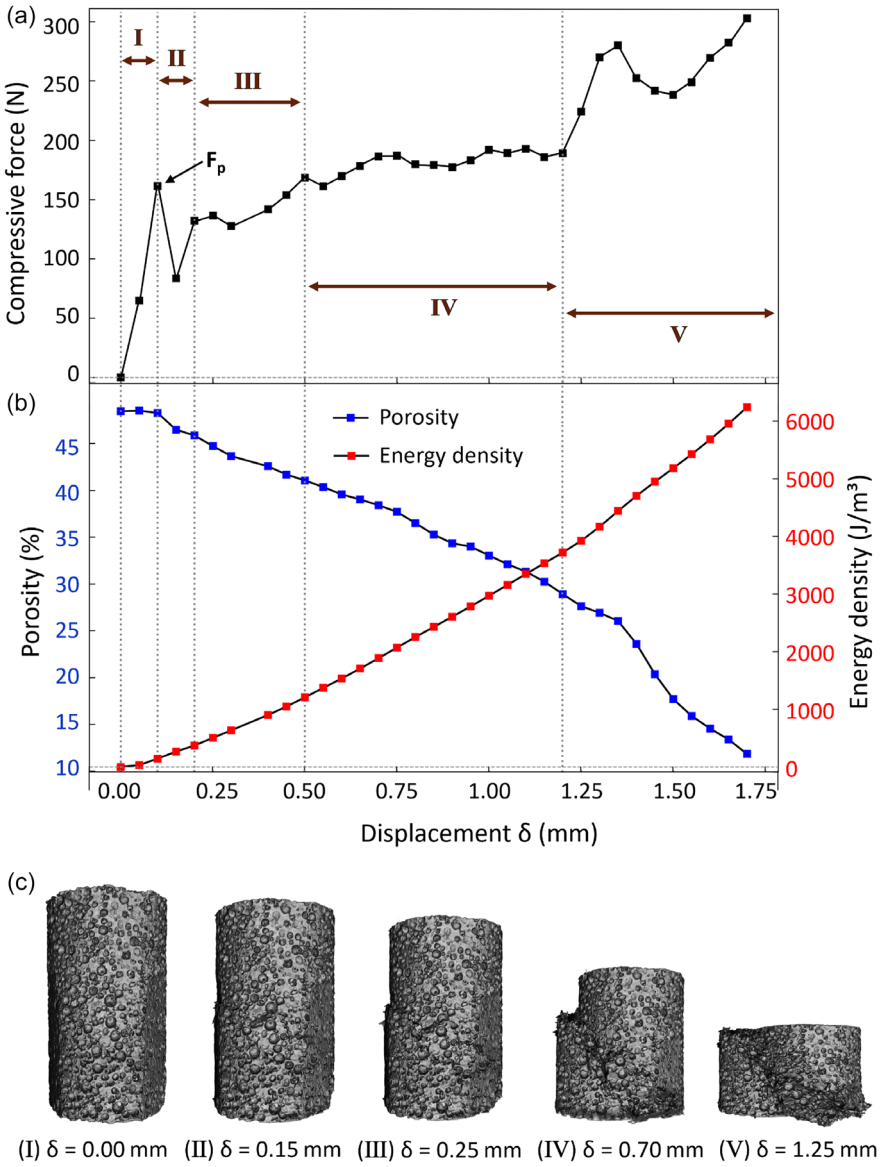

Figure 6. a) Force-versus-displacement response for the in situ compression experiment. The compressive displacement was held fixed after each 0.05 mm step to allow for tomographic scanning of the sample. b) Porosity and energy density plotted versus displacement. The plots are divided into five main parts showing different mechanical response, represented by the gray dotted lines: (I) 0 mm to 0.1 mm, (II) 0.1 mm to 0.2 mm, (III) 0.2 mm to 0.5 mm, (IV) 0.5 mm to 1.2 mm, and (V) 1.2 mm to 1.7 mm. c) The 3D reconstructed MMSF volume, corresponding to a selected displacement step in each deformation stage.

In the fifth region (1.2 mm to 1.7 mm), densification of the sample took place, as shown in Figure 6c and 7h. Toward the end of this process, the cavities of broken CHSs were filled in by matrix material. The porosity rapidly decreased in this region, which can be attributed to a reduction of total void volume through the crushing of CHSs. This stage refers to densification.

3.3. Breakage Evolution of the CHSs

Figure 8 illustrates how the size distribution of intact CHSs gradually evolves during different stages of compressive deformation. As the loading increases, the eventual breaking of CHSs leads to a decrease in the number of intact CHSs. Thus, by studying the evolution of the shape of the size distribution, mean, and standard deviation of the CHS inner diameter, any size preference toward breakage will be revealed.

By close inspection of the size distribution in Figure 8a, it is found that the shape of the distribution remains nearly unchanged throughout the test, with the amplitude mostly changing as the level of compression increases (since the broken spheres are not included in this analysis). From Figure 8b it can be noted that the mean diameter and standard deviation of the size distribution also remain almost constant during the first four stages of deformation. As the compression progresses to

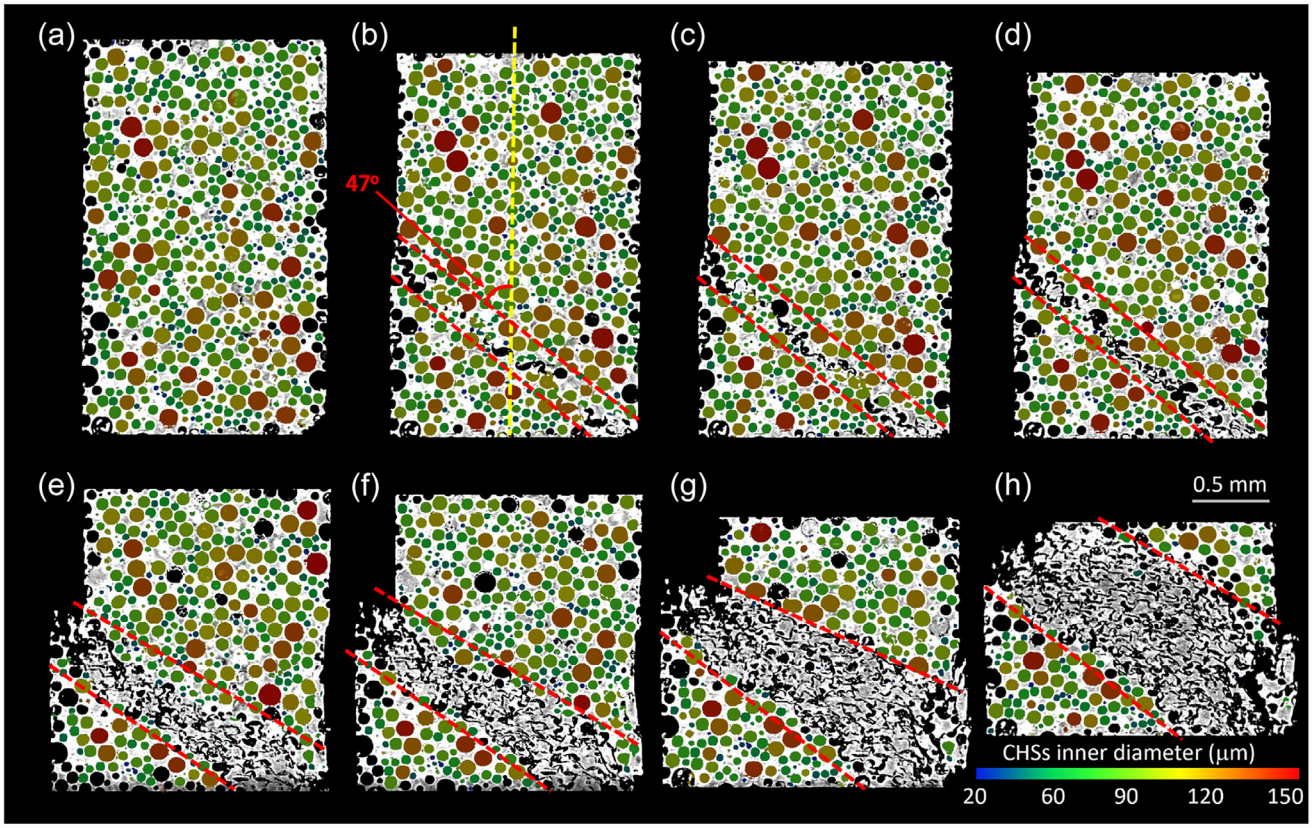

Figure 7. Cross sections through tomographic reconstructions of the MMSF at various stages of compression. Front view of the sample (middle plane) during loading at displacements a) 0.1 mm, b) 0.15 mm, c) 0.20 mm, d) 0.25 mm, e) 0.55 mm, f) 0.65 mm, g) 0.95 mm, and h) 1.25 mm. The color map in the figure legend represents the equivalent-sphere inner diameter of intact filler CHSs. Regions highlighted by dashed red lines encompass the shear band region where CHSs are crushed. The plane of the crack makes an angle of $\psi \approx 47°$ with the applied load direction.

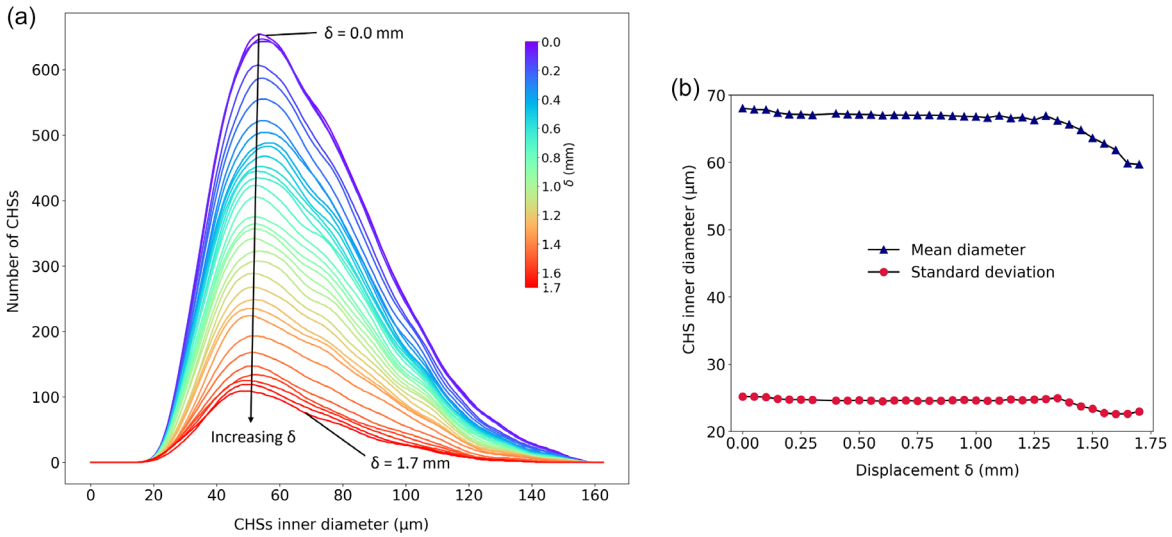

Figure 8. a) Size distribution of CHSs plotted for various states of compressive loading, with δ denoting the displacement. The plot shows the number of intact CHS of different diameters during the compression test, with each curve recorded after an increment of 50 μm in compression. b) Mean and standard deviation of CHS inner diameter distribution, plotted versus displacement δ.

the densification stage (V), a shift in the mean toward smaller diameters (65 μm to 58 μm) is observed. In Figure 7 it is seen that the CHSs are crushed only in the shear band region. The resulting crack was localized spatially, and it linked several CHSs. Based on the results, we cannot conclude that there was preferential size dependent breaking of CHSs. Instead, the behavior suggests that the subsequent widening of the deformation zone remains primarily governed by the location of the shear band. This also indicates that when the CHS size distribution is homogeneous and the deformation is localized within a narrow shear band, a location-dependent nature of failure is observed. A similar localized deformation mechanism has been seen in aluminum syntactic foams during compression[36] and in a study of epoxy syntactic foams.[38] In Ref. [38] localized fracture was attributed to the stiffness of the matrix material. A stiffer matrix was found to limit the redistribution of the applied load; thus, the matrix could not accommodate the high strains induced by the rupture of the first sphere. As a result, stress becomes concentrated at the interfaces between microspheres, leading to a cascading failure where the rupture of one sphere facilitates the crack propagation to its neighbors, regardless of their size. For more compliant matrix materials, the stress distribution was found to be more uniform, leading to preferential failure of the larger microspheres.[38]

Figure 6b shows that significant energy is absorbed during shear fracture propagation. From this, it can be concluded that the localized damage of CHSs is the primary reason for energy absorption even after a crack is initiated in the sample. However, it is also likely that other energy dissipation mechanisms, such as matrix deformation and friction, contribute to the overall energy dissipation. The observed deformation sequence (elastic regime, shear band initiation, sequential CHS rupture, and densification) is consistent with prior studies carried out on larger MMSF specimens,[7] suggesting that the fundamental mechanisms are preserved even for the small sample studied here.

3.4. Mechanical Properties

The mechanical properties of the investigated MMSF, determined from the experimental data, are summarized in **Table 3**.

These values quantify the mechanical performance, and they form the basis for determining potential applications of AlSi12 MMSFs in various structural and engineering contexts. We emphasize that the compressive strength of MMSFs is much higher than typical values for aluminum-based open-cell (1–10 MPa) and closed-cell foams (5–30 MPa).[55,56] Normally, the porosity of traditional Al foams may vary from 50 vol.% to 90 vol.%, or even higher. For MMSFs, however, the porosity is usually between 30 and 65 vol.%. This is mainly a consequence of using a second-phase filler material (CHSs) in foam production. The presence of CHSs gives better control over the geometry of the pores, which also contributes to improved strength and energy absorption. With respect to materials properties, MMSFs are stronger and stiffer than open-cell foams but are usually less ductile. MMSFs also exhibit higher strength and greater energy absorption capability than many closed-cell foams.[55,56]

Table 3. Mechanical properties determined from the experiment.

Compressive strength (σ_c)	86 MPa
Fracture strain (ε_f)	3.70%
Structural stiffness (E_s)	2.32 ± 0.2 GPa
Absorbed elastic energy (U_{el})	149 J m^{-3}
Critical resolved shear stress (τ_{CRSS})	28.0 ± 0.1 MPa

The results of our study provide several different forms of direct input to the validation of predictive modeling schemes. First, the in situ synchrotron tomography measurements enable tracking of 3D microstructural evolution, such as sequential collapse of CHSs, shear band formation, and densification at well-defined load increments. These observations provide a chronological sequence of damage events that can be directly compared with predictions from micromechanical or finite element-based simulations of MMSFs. Second, the correlation of these 3D damage mechanisms with macroscopic quantities (force-displacement response, porosity evolution, and absorbed energy density) provides a quantitative link between local microstructural failure and global materials behavior. This multiscale correlation offers modelers not only stress–strain benchmarks but also microstructure descriptors (e.g., crack initiation sites, shear band inclination, and CHS breakage statistics) that are crucial for calibrating and validating constitutive and damage models. Finally, the finding that CHS rupture is spatially correlated but independent of size adds an important constraint for modeling assumptions regarding load redistribution and crack propagation in syntactic foams. Predictive schemes that incorporate such experimentally observed mechanisms can thus be tested against our dataset to assess their ability to capture both the macroscopic response and the underlying failure sequence.

The present study was restricted to relatively small specimens and a single foam composition, which may limit the generality of absolute property values. Ongoing work is aimed at (i) quantitative comparison with micromechanical and finite element models, (ii) testing larger samples and varying CHS volume fractions to further assess scale effects and broaden applicability, and (iii) in situ X-ray tomography combined with digital volume correlation to map 3D local strain fields and track individual hollow spheres throughout loading for detailed validation of the internal damage mechanism. We acknowledge that future studies on larger volumes would be valuable to further confirm the absence of size effects on quantitative properties.

4. Summary and Conclusions

This study used in situ synchrotron X-ray tomography to investigate the compressive deformation of AlSi12 MMSFs with 64 vol.% CHSs. The deformation was governed by shear band formation and sequential rupture of CHSs, which dissipated energy while maintaining structural integrity during early loading stages. The evolution of porosity correlated closely with the force-displacement response, allowing the deformation to be divided into five distinct stages from elastic loading to final densification. CHS rupture was found to be strongly location-dependent (within the shear band) rather than size-dependent, with spheres of all diameters failing to a similar extent. These results provide mechanistic insight into the interplay between

microstructural damage and macroscopic response, and they form a basis for validating predictive modeling approaches.

Acknowledgements

The authors gratefully acknowledge support provided through the Röntgen-Ångström Cluster program. This research was co-funded by the Swedish Research Council (Vetenskapsrådet) under grant 2021-05959, the Crafoord Foundation (project ID 20230630), and the German Federal Ministry of Education and Research (BMBF) under grant 05K22VUA. P.A.T. Olsson acknowledges funding from the Swedish Research Council under grant 2022-04497. H. Hallberg acknowledges funding from the Swedish e-Science collaboration, under grant eSSENCE@LU 10:1, and from the strategic innovation program LIGHTer, provided by the Swedish Innovation Agency. Parts of this work were supported by the Hungarian Scientific Research Fund under Grant agreement OTKA FK_21 138505. The authors are grateful to DESY (Hamburg, Germany), a member of the Helmholtz Association HGF, for the provision of experimental facilities and beamtime. Parts of this research were carried out at PETRA III P21.2 (The Swedish Materials Science Beamline), with beamtime allocated via proposal 11018445.

Conflict of Interest

The authors declare no conflict of interest.

Data Availability Statement

The data that support the findings of this study are available from the corresponding author upon reasonable request.

Keywords

damage mechanisms, energy absorption, metal matrix syntactic foams, X-ray tomography

Received: June 3, 2025
Revised: November 3, 2025
Published online:

[1] N. Babcsán, D. Leitlmeier, J. Banhart, *Colloids Surf. A Physicochem. Eng. Asp.* **2005**, *261*, 123.
[2] N. Babcsán, F. García Moreno, J. Banhart, *Colloids Surf. A Physicochem. Eng. Asp.* **2007**, *309*, 254.
[3] B. Mehta, Y. Zhao, *Adv. Eng. Mater.* **2024**, *26*, 2400670.
[4] Z. Huang, C. Hu, L. Shen, Y. Wang, B. Wang, F. Ye, Q. Liu, *Mater. Sci. Eng. A* **2023**, *872*, 144942.
[5] A. Motaharinia, J. W. Drelich, J. Goldman, H. R. Bakhsheshi-Rad, S. Sharif, A. F. Ismail, M. Razzaghi, *J. Mater. Res. Technol.* **2024**, *30*, 8316.
[6] G. Parande, D. J. E. Chow, A. P. Sripathy, V. Manakari, M. Doddamani, M. Gupta, *J. Mater. Eng. Perform.* **2024**, *33*, 12160.
[7] I. N. Orbulov, J. Ginsztler, *Compos. A: Appl. Sci. Manuf.* **2012**, *43*, 553.
[8] E. Linul, D. Pietras, T. Sadowski, L. Marşavina, D. K. Rajak, J. Kovacik, *Compos. A: Appl. Sci. Manuf.* **2021**, *149*, 106516.
[9] J. Marx, M. Portanova, A. Rabiei, *J. Compos. Sci.* **2020**, *4*, 176.
[10] M. Garcia-Avila, M. Portanova, A. Rabiei, *Compos. Struct.* **2015**, *125*, 202.
[11] D. P. Mondal, N. Jha, A. Badkul, S. Das, R. Khedle, *Mater. Sci. Eng. A* **2012**, *534*, 521.
[12] T. Fiedler, K. Al-Sahlani, P. A. Linul, E. Linul, *J. Alloys Compd.* **2020**, *813*, 152181.
[13] I. N. Orbulov, A. Szlancsik, *Adv. Eng. Mater.* **2018**, *20*, 1700980.
[14] *Metal Matrix Syntactic Foams: Processing, Microstructure, Properties and Applications* (Eds: N. Gupta, P. K. Rohatgi), DEStech Publications, Inc **2014**.
[15] M. Kiser, M. Y. He, F. W. Zok, *Acta Mater.* **1999**, *47*, 2685.
[16] A. Daoud, *Mater. Sci. Eng. A* **2008**, *488*, 281.
[17] C. Kádár, K. Máthis, I. N. Orbulov, F. Chmelík, *Mater. Lett.* **2016**, *173*, 31.
[18] C. Kádár, A. Szlancsik, Z. Dombóvári, I. N. Orbulov, *Mater. Lett.* **2019**, *257*, 126733.
[19] W. S. Sanders, L. J. Gibson, *Mater. Sci. Eng. A* **2003**, *347*, 70.
[20] P. R. Marur, *Mater. Lett.* **2005**, *59*, 1954.
[21] P. R. Marur, *Comput. Mater. Sci.* **2009**, *46*, 327.
[22] W. Yu, Q. Meng, L. Xi, H. Li, *Ceram.-Silikáty* **2016**, *60*, 77.
[23] L. Pérez, M. Villalobos, C. Órdenes, R. A. L. Drew, C. Ruiz-Aguilar, I. Alfonso, *J. Mater. Eng. Perform.* **2019**, *28*, 100.
[24] E. Maire, J. Y. Buffière, L. Salvo, J. J. Blandin, W. Ludwig, J. M. Létang, *Adv. Eng. Mater.* **2001**, *3*, 539.
[25] B. J. Connolly, D. A. Horner, S. J. Fox, A. J. Davenport, C. Padovani, S. Zhou, A. Turnbull, M. Preuss, N. P. Stevens, T. J. Marrow, J. Y. Buffiere, E. Boller, A. Groso, M. Stampanoni, *Mater. Sci. Technol.* **2006**, *22*, 1076.
[26] J. Gubicza, K. Nagy, Z. Hegedűs, I. Tambe, P. Nagy, J. Hektor, C. Han, H. Choe, *Mater. Sci. Eng. A* **2025**, *942*, 148673.
[27] S. Wu, P. J. Withers, S. Beretta, G. Kang, *Eng. Fract. Mech.* **2023**, *292*, 109628.
[28] Y. Du, D. Zhang, L. Wang, W. Guo, L. Wang, *J. Eur. Ceram. Soc.* **2024**, *44*, 142.
[29] W. Qian, S. Wu, L. Lei, Q. Hu, C. Liu, *J. Mater. Sci. Technol.* **2024**, *175*, 80.
[30] S. Wu, *Eng. Fract. Mech.* **2025**, *319*, 111036.
[31] D. Zhang, Y. Liu, H. Liu, Y. Feng, H. Guo, Z. Hong, C. Chen, Y. Zhang, *Compos. Struct.* **2021**, *275*, 114447.
[32] W. Guo, D. Zhang, Y. Zhang, Y. Du, C. Chen, *Compos. B: Eng.* **2024**, *279*, 111439.
[33] F. Beckmann, R. Grupp, A. Haibel, M. Huppmann, M. Nöthe, A. Pyzalla, W. Reimers, A. Schreyer, R. Zettler, *Adv. Eng. Mater.* **2007**, *9*, 939.
[34] J. Y. Buffière, E. Maire, P. Cloetens, G. Lormand, R. Fougères, *Acta Mater.* **1999**, *47*, 1613.
[35] C. F. Martin, C. Josserond, L. Salvo, J. J. Blandin, P. Cloetens, E. Boller, *Scr. Mater.* **2000**, *42*, 375.
[36] D. K. Balch, J. G. O'Dwyer, G. R. Davis, C. M. Cady, *Mater. Sci. Eng. A* **2005**, *391*, 408.
[37] T. Bubonyi, P. Barkóczy, A. Kemény, Z. Gácsi, *Compos. A: Appl. Sci. Manuf.* **2024**, *185*, 108292.
[38] J. Adrien, E. Maire, N. Gimenez, V. Sauvant-Moynot, *Acta Mater.* **2007**, *55*, 1667.
[39] J. Lachambre, E. Maire, J. Adrien, D. Choqueuse, *Acta Mater.* **2013**, *61*, 4035.
[40] S. Youssef, E. Maire, R. Gaertner, *Acta Mater.* **2005**, *53*, 719.
[41] J. Y. Chen, Y. Huang, M. Ortiz, *J. Mech. Phys. Solids* **1998**, *46*, 789.
[42] S. Pal, S. Maiti, G. Subhash, *Mech. Mater.* **2010**, *42*, 118.
[43] Y. Zhang, Y. Wang, C. Q. Chen, *J. Mech. Phys. Solids* **2019**, *123*, 28.
[44] J. Y. Buffière, P. Cloetens, W. Ludwig, E. Maire, L. Salvo, *MRS Bull.* **2008**, *33*, 611.
[45] I. N. Orbulov, *Mater. Sci. Eng. A* **2013**, *583*, 11.
[46] Z. Hegedüs, T. Müller, J. Hektor, E. Larsson, T. Bäcker, S. Haas, A. L. C. Conceiçao, S. Gutschmidt, U. Lienert, In *40th Risø*

International Symposium on Materials Science: Metal Microstructures in 2D, 3D and 4D **2019**, Vol. *580*, pp. 012032.
[47] B. A. Dowd, G. H. Campbell, R. B. Marr, V. V. Nagarkar, S. V. Tipnis, L. Axe, D. P. Siddons, In *SPIE's Inter. Symp. on Optical Science, Engineering, and Instrumentation* **1999**, Vol. *3772*, pp. 224–236.
[48] D. Gürsoy, F. De Carlo, X. Xiao, C. Jacobsen, *J. Synchrotr. Radiati.* **2014**, *21*, 1188.
[49] Avizo 2022 [Computer software] 2025. "Thermo Fisher Scientific" https://www.thermofisher.com, Accessed: October 2025.
[50] P. Virtanen, R. Gommers, T. E. Oliphant, M.Haberland, T. Reddy, D. Cournapeau, E. Burovski, P. Peterson, W. Weckesser, J. Bright, S. J. Walt, M. Brett, J. Wilson, K. J. Millman, N. Mayorov, A. R. J. Nelson, E. Jones, R. Kern, E. Larson, C. J. Carey, I. Polat, Y. Feng, E. W. Moore, J. VanderPlas, D. Laxalde, J. Perktold, R. Cimrman, I. Henriksen, E. A. Quintero, C. R. Harris, et al., *Nat. Methods* **2020**, *17*, 261.
[51] R. Rorato, M. Arroyo, E. Andò, A. Gens, *Eng. Geol.* **2019**, *254*, 43.
[52] H. Wadell, *J. Geol.* **1932**, *40*, 443.
[53] Dragonfly 2022.2 [Computer software] 2025. "Comet Technologies Canada Inc." https://www.theobjects.com/dragonfly, Montreal, Canada; Accessed: October 2025.
[54] N. Gupta, Kishore, E. Woldesenbet, S. Sankaran, *J. Mater. Sci.* **2001**, *36*, 4485.
[55] M. F. Ashby, A. G. Evans, N. A. Fleck, L. J. Gibson, J. W. Hutchinson, H. N. G. Wadley, *Metal Foams: A Design Guide*, Butterworth-Heinemann, Oxford, UK **2000**.
[56] L. J. Gibson, M. F. Ashby, *Cellular Solids: Structure and Properties, Cambridge Solid State Science Series*, Cambridge University Press, Cambridge, UK **1997**.
[57] S. Siddique, *Reliability of Selective Laser Melted AlSi12 Alloy for Quasistatic and Fatigue Applications*, Springer Vieweg, Wiesbaden, Germany **2019**, pp. 65–76.